SUPPLEMENTARY INFORMATION

Three-dimensional synchronous proton radiography for dynamic magnetic fields in laser-produced high-energy-density plasmas

Z. H. Zhao†,[1] S. K. He†,[2] H. H. An†,[3] Z. Lei,[1] Y. Xie,[1] W. Q. Yuan,[1] J. L. Jiao,[1] K. N. Zhou,[2] J. J. Ye,[3] Z. Y. Xie,[3] J. Xiong,[3] Z. H. Fang,[3] X. T. He,[4] W. Wang,[3] W. M. Zhou,[2] B. H. Zhang,[2] S. P. Zhu✉,[2,4] and B. Qiao✉[1]

[1)] *Center for Applied Physics and Technology, HEDPS, and SKLNPT, School of Physics, Peking University, Beijing 100871, China*

[2)] *Science and Technology on Plasma Physics Laboratory, Research Center of Laser Fusion, China Academy of Engineering Physics (CAEP), Mianyang 621900, China*

[3)] *Shanghai Institute of Laser Plasma, CAEP, Shanghai 201800, China*

[4)] *Institute of Applied Physics and Computational Mathematics, Beijing 100094, China*

(Dated: 2 September 2021)

STATIC 3D PROTON RADIOGRAPHYS

The high-spatial resolution ($\sim$ 10 μm) of proton radiography originates from the uniform laminar proton beam produced by target normal sheath acceleration (TNSA) with relativistic ps and fs laser pulses. Figure **S1** shows the static 3D proton radiographs for the mesh-grid only in our experiments, where the upper row is from the face-on direction and the lower row is from the side-on direction. It can be seen that the mesh grids on all radiographs are clear and distinguishable for up to 6 RCFs, which implies that the proton beams are almost uniform with cut-off energies more than 8 MeV. Moreover, there are almost no mutual inferences between the face-on and side-on probing proton beams. Therefore, such high-quality uniform proton beams are fully capable of achieving the dynamic 3D synchronous radiography.

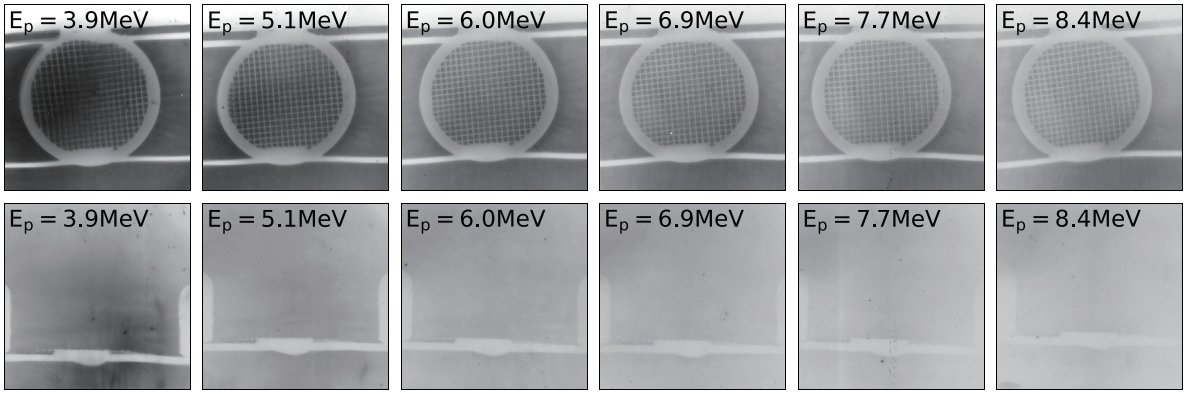

Fig S1. Static 3D synchronous proton radiography for mesh-grids, where the upper row is from the face-on direction driven by the ps pulse and the lower row is from the side-on direction driven by the fs pulse.

HED PLASMA PARAMETERS OBTAINED FROM RMHD SIMULATIONS

To obtain the detailed HED CH/Cu plasma parameters, we used the RMHD code FLASH to simulate the whole laser irradiation process of the solid foil target. The detailed simulation setup can be seen in the Methods. Figure **S2** plots distributions of the obtained electron densities n_e, electron temperatures T_e and ion charge states $\bar{Z}$ of respectively laser-produced CH and Cu plasmas at time t = 1.8 ns. It shows that the CH [**S2**(a)] and Cu [**S2**(d)]

† These authors have contributed to this work equally.
✉ Corresponding author. e-mail: bqiao@pku.edu.cn, zhu_shaoping@iapcm.ac.cn.

plasmas have similar electron density distributions, which drops from 10^{22} cm^{-3} near the laser focal spot to 10^{19} cm^{-3} in the coronal region. From the outline of the electron density distributions, the expansion velocities are estimated as $v_z \sim 1000$ km/s and $v_x \sim 600$ km/s for CH plasmas, and those for Cu plasmas are slightly faster. We also see that the temperature in Cu [**S2**(e)] plasmas is higher than that in CH plasmas [**S2**(b)], and for both cases the temperature gradients decrease with the distance away from the laser focal spot up to a few hundred microns, after which the temperature distributions are almost uniform. Note that there exist a non-physical shock heating in the plasma front because in RMHD simulation a background plasma has to be set initially, however, this is too weak to cause any impact on the interior plasmas. As far as the ion charge states $\bar{Z}$ to be concerned, we see that the low-Z CH plasmas [**S2**(c)] is almost fully ionized as $\bar{Z}_{\rm CH} \sim 3.5$, while the high-Z Cu plasmas [**S2**(f)] are ionized to $\bar{Z}_{\rm Cu} \sim 25$ near the focal spot, which drops to about 18 in the corona region.

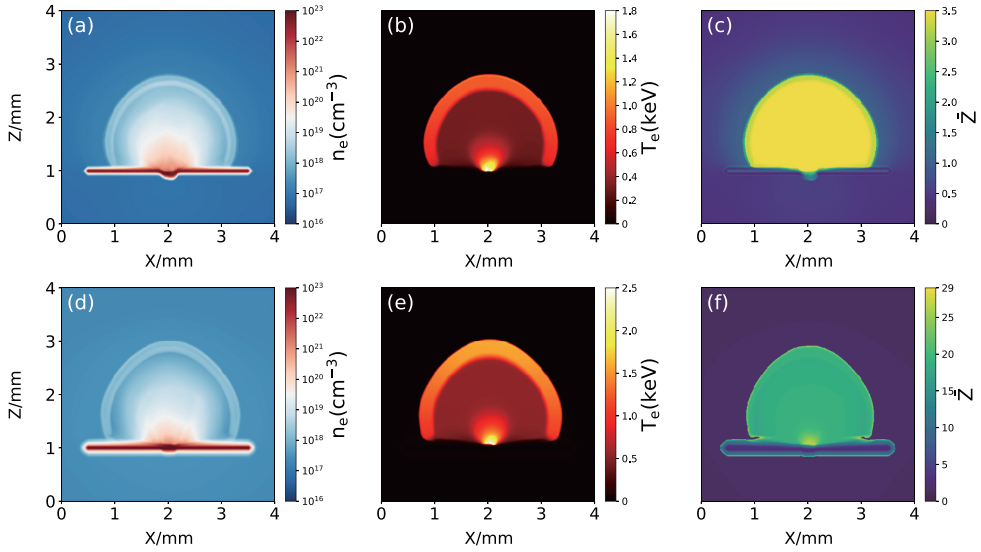

Fig S2. Distributions of the electron densities n_e [(a) and (d)], electron temperatures T_e [(b) and (e)] and ion charge states $\bar{Z}$ [(c) and (f)] of respectively laser-produced CH (the upper row) and Cu (the lower row) plasmas at time $t = 1.8$ ns obtained from RMHD simulations.

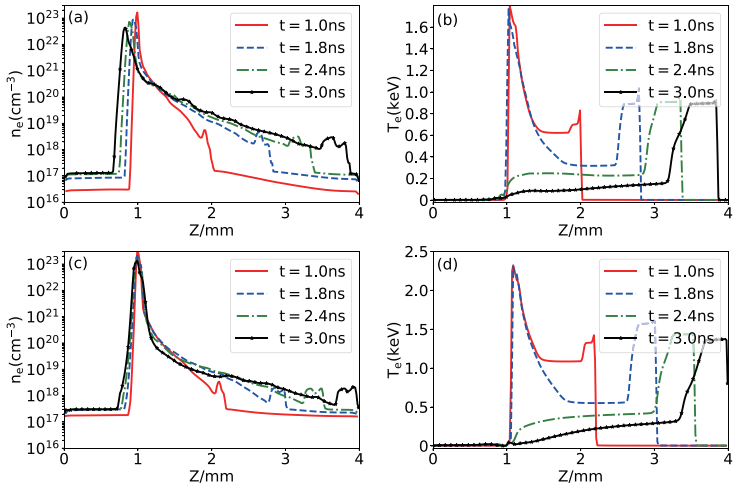

Fig S3. Profiles along z-axis of electron densities n_e [(a) and (c)] and temperatures T_e [(b) and (d)] of of respectively laser-produced CH (the upper row) and Cu (the lower row) plasmas at times $t = 1.0$, 1.8, 2.4 and 3.0 ns obtained from RMHD simulations.

Figure **S3** plots the profiles along z-axis of electron densities n_e and temperatures T_e of respectively laser-produced CH and Cu plasmas at different times. We see that all densities [**S3**(a) and **S3**(c)] exhibit an exponentially decreasing profile, which imply that both plasmas experiences a self-similar expansion. The density gradient lengths l_n =

$1/\left(\frac{\mathrm{d}\ln(n_e)}{\mathrm{d}z}\right)$ of CH and Cu plasmas can be estimated as $l_{n,\mathrm{CH}} \sim 450$ μm and $l_{n,\mathrm{Cu}} \sim 600$ μm. For typical plasma densities $10^{19}\mathrm{cm}^{-3} < n_e < 10^{20}\mathrm{cm}^{-3}$ in our experiments, the gradient length is about a few to ten times of the ion skin depth d_i. The temperature gradient lengths $l_T = 1/\left(\frac{\mathrm{d}\ln(T_e)}{\mathrm{d}z}\right)$ for both CH and Cu plasmas are about 500 μm.

Figure **S4** shows the electron-ion collision time $\tau_{ei} = \frac{3m_e^{1/2}T_e^{1/2}}{4\sqrt{2\pi}n_i Z^2 e^4 \ln\Lambda}$ at different positions z of respectively laser-produced CH and Cu plasmas evolving with time. We see that for all cases τ_{ei} is a few ps near the solid foil target (at $z = 1$ mm) for a few hundred microns, and then increases to tens of ps outside the plasma bubble, due to the exponential decrease of electron density [Fig. **S3**]. This time is less than or close to the characteristic time of plasma evolution, i.e., the role of collision effect in some plasma processes (e.g., kinetic instabilities) cannot be ignored.

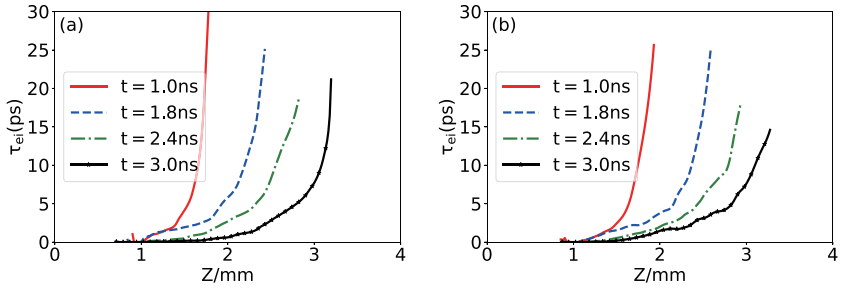

Fig S4. The electron-ion collision time τ_{ei} at different positions z of respectively laser-produced CH (a) and Cu (b) plasmas at different times.

LOCAL CHARACTERISTIC TIME OF PLASMAS IN COLLISIONAL PIC SIMULATION

In the collisional PIC simulations, to evaluate the growth rate of the Weibel instabilities more accurately, we calculate the local characteristic time $t_{loc} = L_{loc}/v_{Te,loc}$, where L_{loc} and $v_{Te,loc}$ are the local temperature gradient length and electron thermal velocity. Figure **S5** show the radial profiles of the normalized local characteristic times $t_{loc}v_{Te0}/L_0 = (L_{loc}/v_{Te,loc})/(L_0/v_{Te0})$ of respectively the collisionless ($\alpha = 0$), CH ($\alpha = 20$) and Cu ($\alpha = 40$) plasmas in the PIC simulations at time $t = 10l_{T0}/v_{Te0}$. We see that the local characteristic time decreases while the collision effect increases, which is because that the collision effects inhibit the mobility of hot electrons and cause the decrease of the electron thermal conductivity, being beneficial to maintain a steeper electron temperature gradient (smaller L_{loc} and larger $v_{Te,loc}$). Despite these differences, the normalized characteristic time t_{loc} of CH ($\alpha = 20$) and Cu ($\alpha = 40$) plasmas are both on the order of 10. This indicates that the difference of the collisional effect does not change plasma spatial distributions significantly, so the differences in the evolutions of self-generated magnetic fields are mainly due to the differences in the momentum spaces, i.e., the kinetic Weibel instabilities.

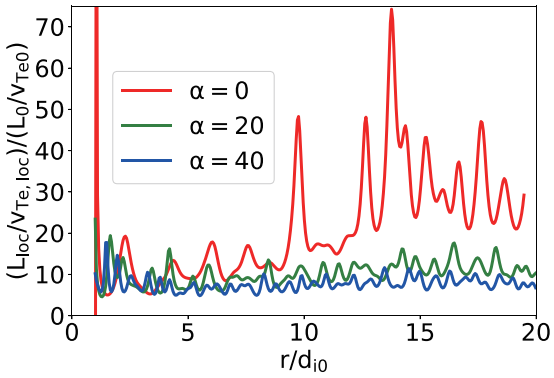

Fig S5. The radial profiles of the normalized local characteristic times $(t_{loc}v_{Te0})/L_0 = (L_{loc}/v_{Te,loc})/(L_0/v_{Te0})$ of respectively the collisionless ($\alpha = 0$), CH ($\alpha = 20$) and Cu ($\alpha = 40$) plasmas in PIC simulations at time $t = 10l_{T0}/v_{Te0}$.

HED PLASMA PARAMETERS IN VFP SIMULATIONS

Figures S6(a) and S6(b) show the initial electron density distributions of respectively CH and Cu plasmas in the VFP simulations, which matches well with those obtained from the RMHD simulations (Figs. S2 and S3). They both decrease with the distance away from the solid foil target, where the critical density surface ($n_e \sim 4 \times 10^{21}$ cm^{-3}) is at about 150 μm away, and then down to about $n_e \sim 1 \times 10^{20}$ cm^{-3} at 300 μm away [see the gray lines in S6(a) and S6(b)]. Also, the average charge states of CH and Cu plasmas are set to be $\bar{Z}_{\rm CH} = 3.5$ and $\bar{Z}_{\rm Cu} = 25$, respectively, following those obtained from RMHD. Similarly to RMHD, a laser with intensity of 4×10^{15} W/cm^2 is used in VFP simulations as the heating source through an inverse bremsstrahlung absorption operator. Figures S6(c)-S6(f) plot the temperature distributions of respectively CH (the left column) and Cu (the right column) plasmas at time $t = 200$ ps [S6(c) and S6(d)] and 300 ps [S6(e) and S6(f)]. We see that as a whole the temperature of Cu plasmas ($T_e \sim 1.8$ keV) is higher than that of CH plasmas (~ 1.0 keV) due to the stronger inverse bremsstrahlung absorption, in consistence with the RMHD simulation results. We also see that generally a steep temperature gradient (∇T_e) exists near the laser focal spot, and the Biermann magnetic field ($\nabla n_e \times \nabla T_e$) will be generated when the electron density gradient (∇n_e) is applied. The electron heat flux $\mathbf{q}_e$ driven by the electron temperature gradient, marked by the white arrows in S6(c)-S6(f), results in advection of the self-generated magnetic fields through the Nernst effect, which, in turn, also react on the electron thermal conductivity through the Righi-Leduc effect. From S6(e) and S6(f), we further see that at 100ps after the end of the laser, although the electron temperature T_e decreases, the electron temperature gradient and the corresponding electron heat flux $\mathbf{q}_e$ still exist. Therefore, it is expected that generation and transport of magnetic fields can still maintain hundreds of ps after the laser is over. Note that here the values of the temperatures in VFP simulations are relatively lower than those in RMHD simulations, which are due to the inconsistent equation of state (EOS) and energy absorption calculations between them.

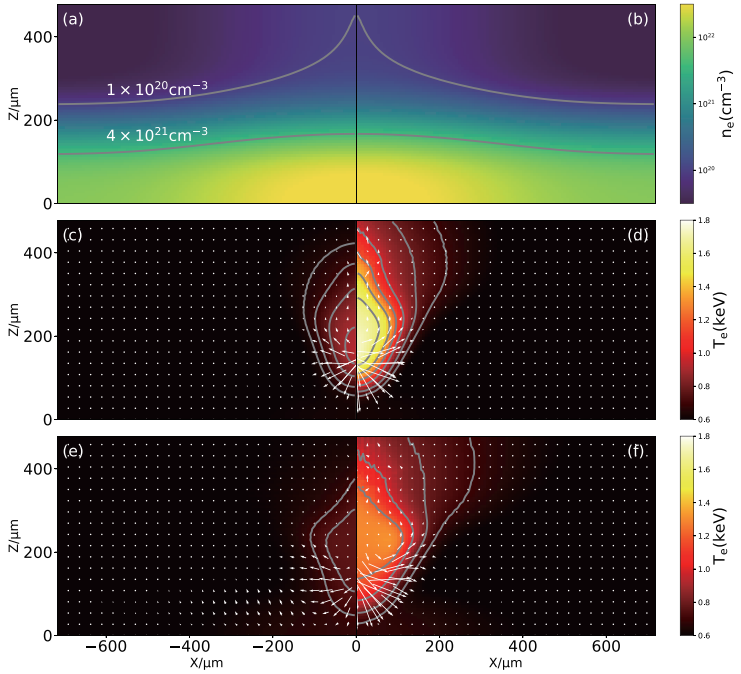

Fig S6. HED plasma parameters in VFP simulations. (a) and (b) the initial electron density distributions of respectively CH and Cu plasmas; (c)-(f) the temperature distributions of respectively CH (the left column) and Cu (the right column) plasmas at time $t = 200$ ps [(c) and (d)] and 300 ps [(e) and (f)]. The white arrows represent the direction of electron heat flow $\mathbf{q}_e$, and the lengths indicate their relative strengths.